

Supplementary Information

Novel entropy-stabilized fluorite oxides with multifunctional properties

Ashutosh Kumar, David Bérardan, Francois Brisset, Diana Dragoe, Nita Dragoe*

ICMMO (UMR CNRS 8182), Université Paris-Saclay, F-91405 Orsay, France

*Email: nita.dragoe@universite-paris-saclay.fr

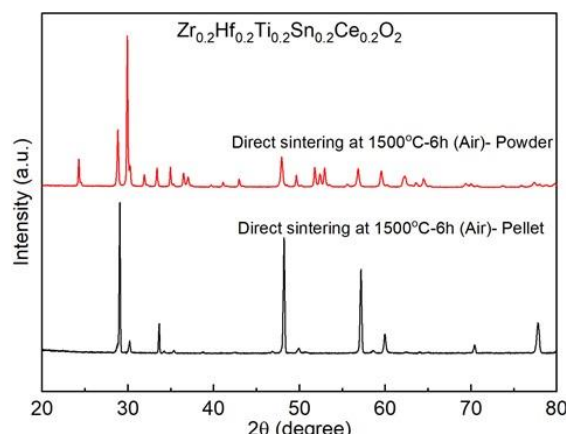


Fig.S1. X-ray diffraction pattern for $Zr_{0.2}Hf_{0.2}Ti_{0.2}Sn_{0.2}Ce_{0.2}O_2$. The mixed precursors are directly sintered at 1500°C for 6h followed by quenching. The difference in the XRD pattern for powder and pellet is seen.

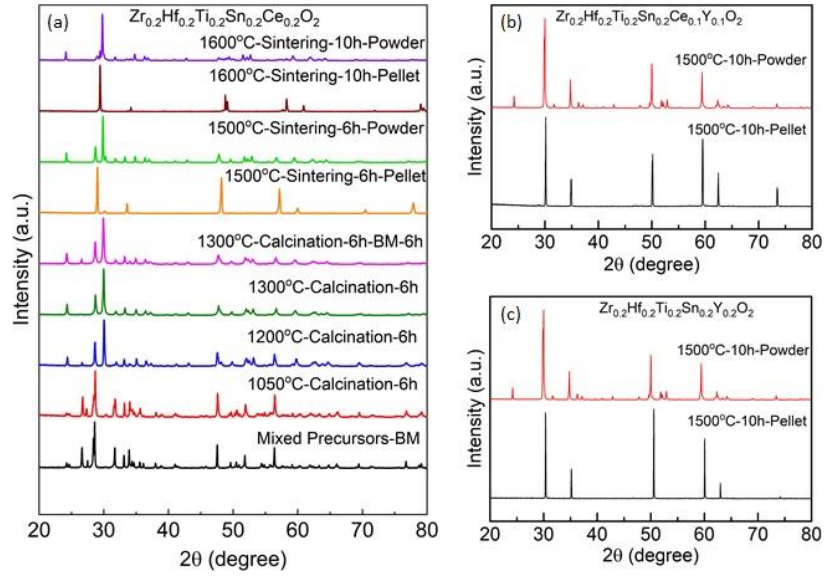


Fig.S2. (a) X-ray diffraction pattern for $Zr_{0.2}Hf_{0.2}Ti_{0.2}Sn_{0.2}Ce_{0.2}O_2$ at each step. The mixed precursors starts reacting at 1200°C and forms an orthorhombic structure. The pellet (surface) shows single fluorite structure; however XRD pattern of the powder shows predominantly orthorhombic structure. Similar nature of XRD pattern of pellet and powder is seen for (b) $Zr_{0.2}Hf_{0.2}Ti_{0.2}Sn_{0.2}Ce_{0.1}Y_{0.1}O_2$, (c) $Zr_{0.2}Hf_{0.2}Ti_{0.2}Sn_{0.2}Y_{0.2}O_2$.

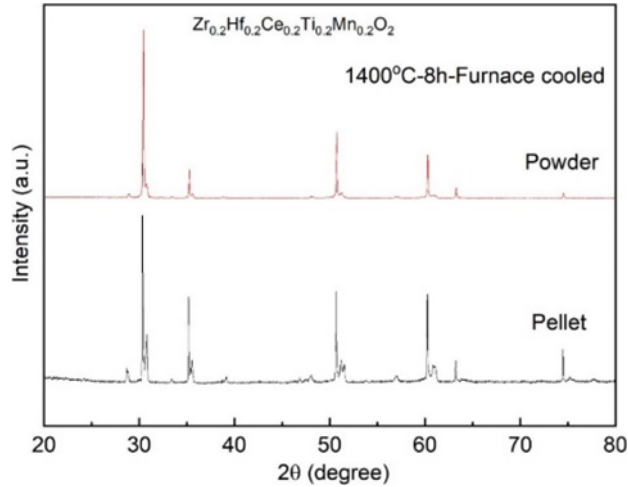


Fig.S3. The X-ray diffraction pattern for $Zr_{0.2}Hf_{0.2}Ce_{0.2}Ti_{0.2}Mn_{0.2}O_2$ sintered at 1400°C for 8 hours followed by furnace cooling. Although, the XRD pattern remain same in pellet and powder. The sample shows secondary phases.

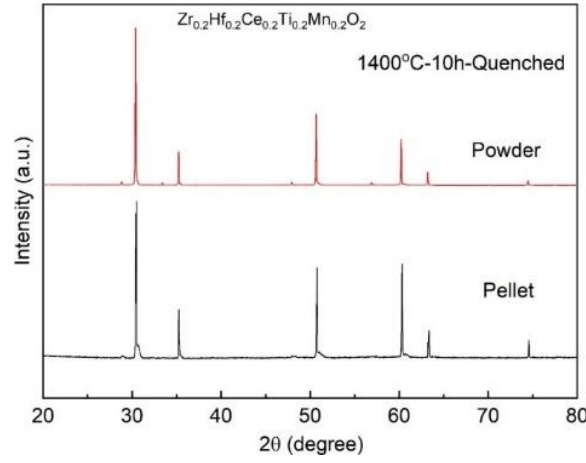


Fig.S4. The X-ray diffraction pattern for $Zr_{0.2}Hf_{0.2}Ce_{0.2}Ti_{0.2}Mn_{0.2}O_2$ sintered at 1400°C for 10 hours followed by quenching (crucible kept outside the furnace). The XRD pattern is close to single phase.

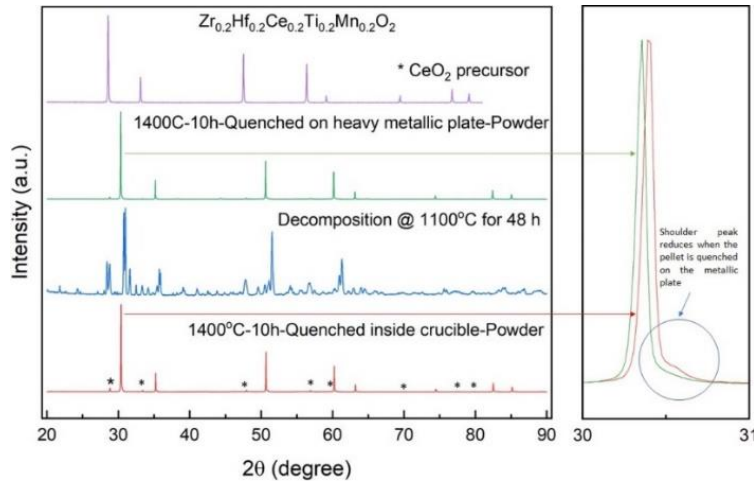


Fig.S5. The X-ray diffraction pattern for $Zr_{0.2}Hf_{0.2}Ce_{0.2}Ti_{0.2}Mn_{0.2}O_2$ sintered at 1400°C for 10 hours followed by quenching on metallic plate. Zoom-in shows the symmetric peak of maximum intensity peak when the sample is cooled faster via quenching on metallic plate.

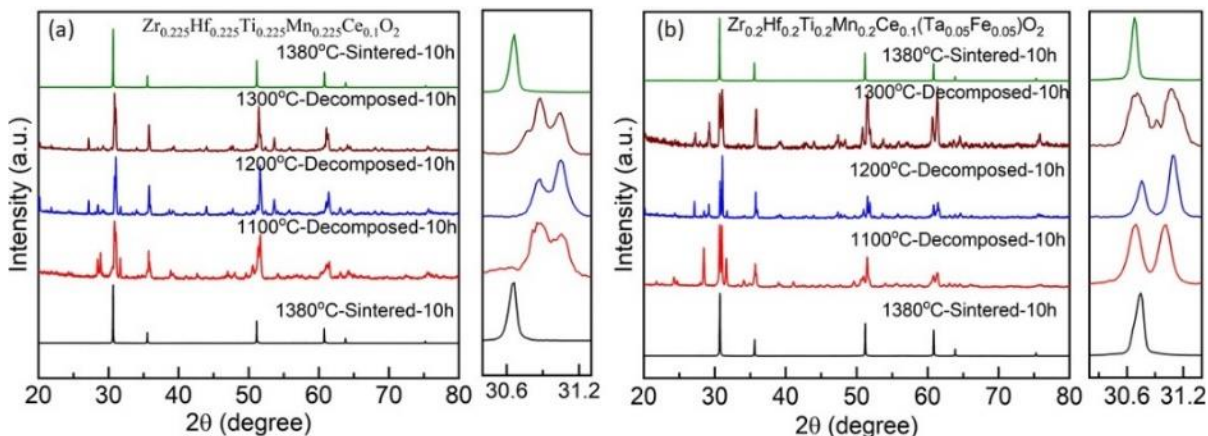


Fig.S6. Temperature evolution of entropy stabilized fluorite structure (a) $Zr_{0.225}Hf_{0.225}Ti_{0.225}Mn_{0.225}Ce_{0.1}O_2$ (b) $Zr_{0.2}Hf_{0.2}Ti_{0.2}Mn_{0.2}Ce_{0.1}(Ta_{0.05}Fe_{0.05})O_2$. The zoom-in image shows the single phase, decomposed phase and reversible single phase.

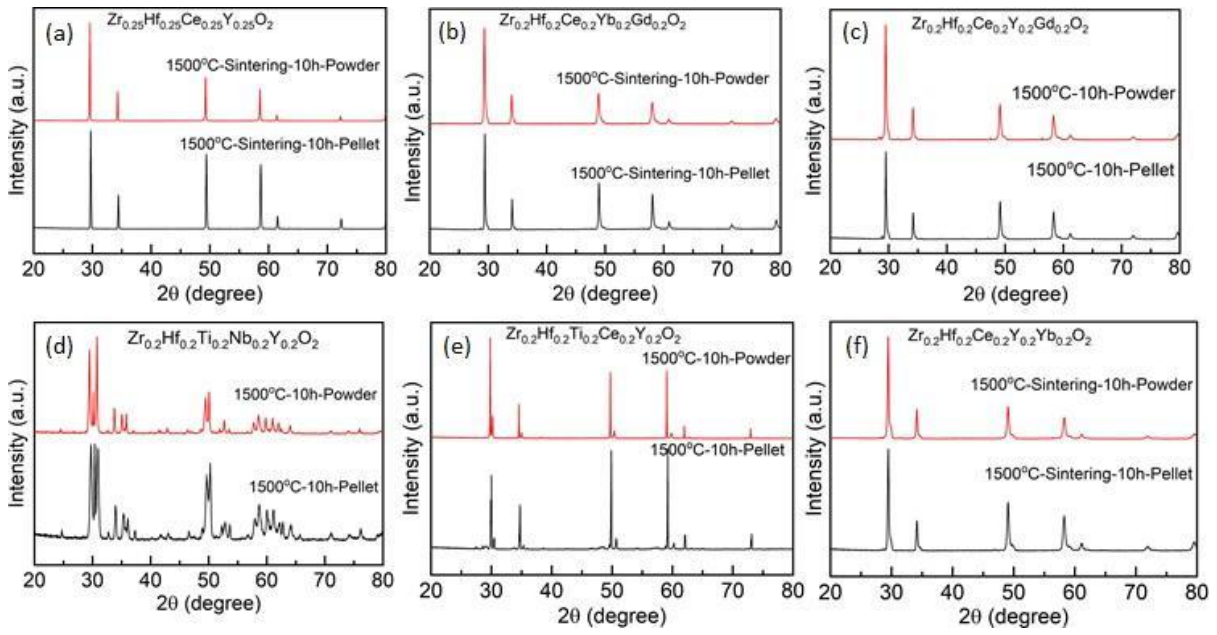


Fig.S7. X-ray diffraction pattern for (a) $Zr_{0.25}Hf_{0.25}Ce_{0.25}O_2$, (b) $Zr_{0.2}Hf_{0.2}Ce_{0.2}Yb_{0.2}Gd_{0.2}O_2$ (c) $Zr_{0.2}Hf_{0.2}Ce_{0.2}Y_{0.2}Gd_{0.2}O_2$ (d) $Zr_{0.2}Hf_{0.2}Ti_{0.2}Nb_{0.2}Y_{0.2}O_2$ (e) $Zr_{0.2}Hf_{0.2}Ti_{0.2}Ce_{0.2}Y_{0.2}O_2$, and (f) $Zr_{0.2}Hf_{0.2}Ce_{0.2}Y_{0.2}Gd_{0.2}O_2$. All the sample shows similar nature of diffraction pattern in both pellet and powder. However, only $Zr_{0.25}Hf_{0.25}Ce_{0.25}O_2$, $Zr_{0.2}Hf_{0.2}Ce_{0.2}Yb_{0.2}Gd_{0.2}O_2$ shows a single-phase fluorite structure.

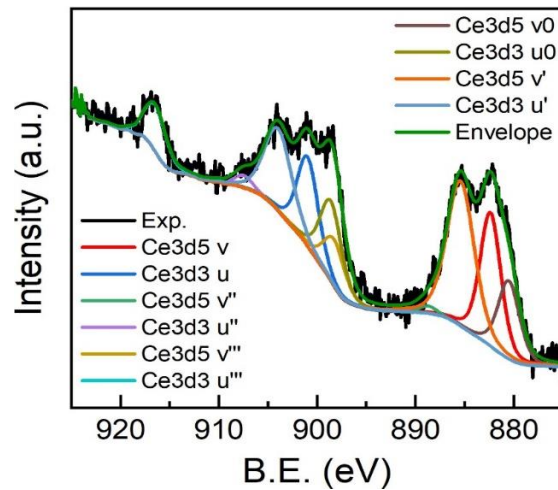


Fig.S8. Core-level Ce-3d peaks of $Zr_{0.2}Hf_{0.2}Sn_{0.2}Ce_{0.2}Ti_{0.2}O_2$ are deconvoluted using CasaXPS software. The details of this fitting are shown in Table S3.

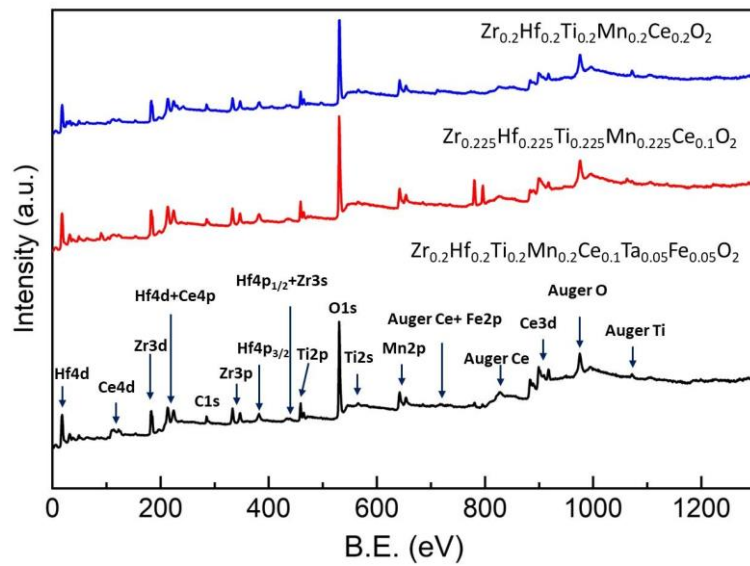


Fig.S9. Full scan X-ray photoelectron spectroscopy of entropy-stabilized fluorites.

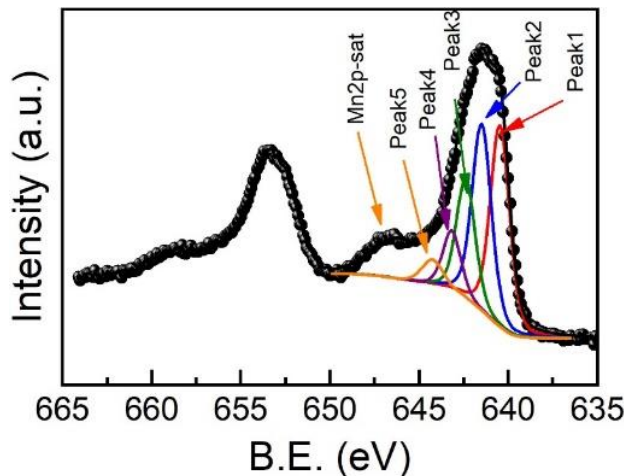


Fig.S10. Core-level Mn-2p peaks are deconvoluted using CasaXPS software. The details of this fitting are shown in Table S4.

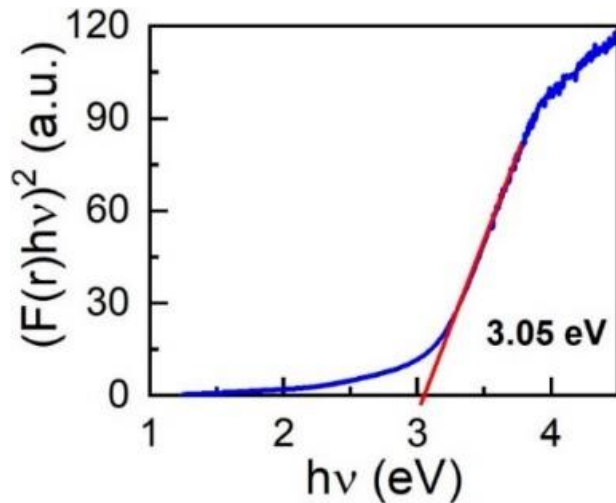


Fig.S11. Band gap obtained from UV-Visible spectroscopy for $Zr_{0.2}Hf_{0.2}Ce_{0.2}Sn_{0.2}Ti_{0.2}O_2$.

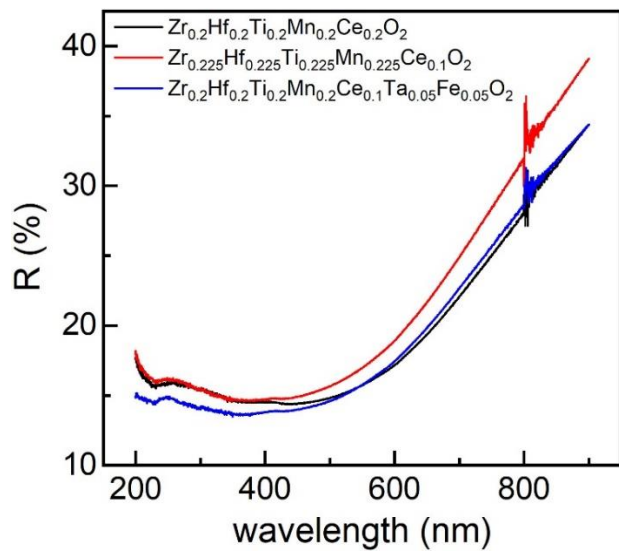


Fig.S12. UV-Visible-NIR spectra for entropy-stabilized fluorite oxides.

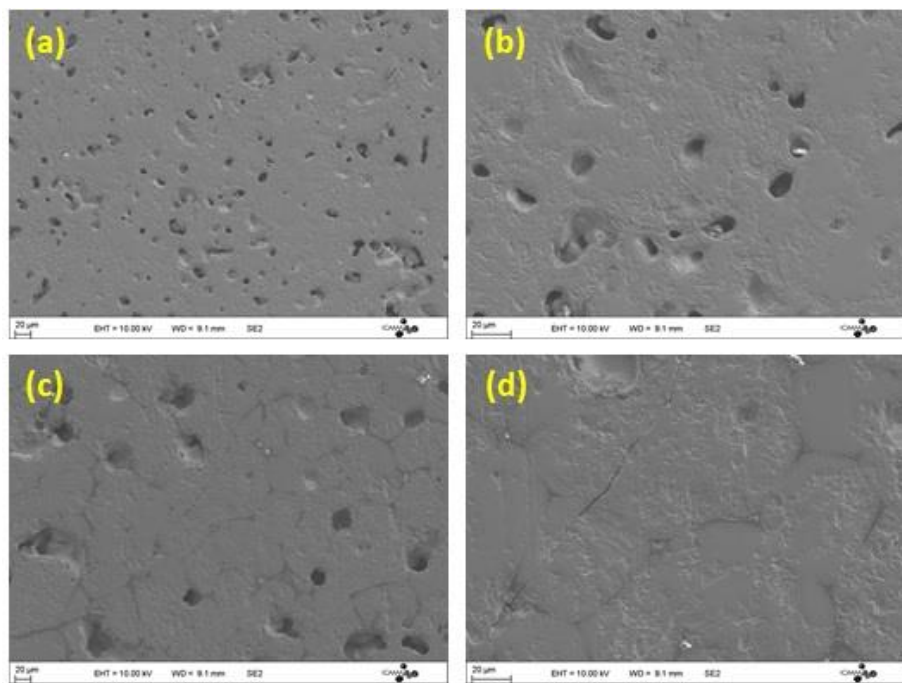


Fig.S13. Scanning electron microscope (SEM) image for (a,b) $\text{Zr}_{0.2}\text{Hf}_{0.2}\text{Ti}_{0.2}\text{Mn}_{0.2}\text{Ce}_{0.2}\text{O}_{2-\delta}$ (c,d) $\text{Zr}_{0.225}\text{Hf}_{0.225}\text{Ti}_{0.225}\text{Mn}_{0.225}\text{Ce}_{0.1}\text{O}_{2-\delta}$.

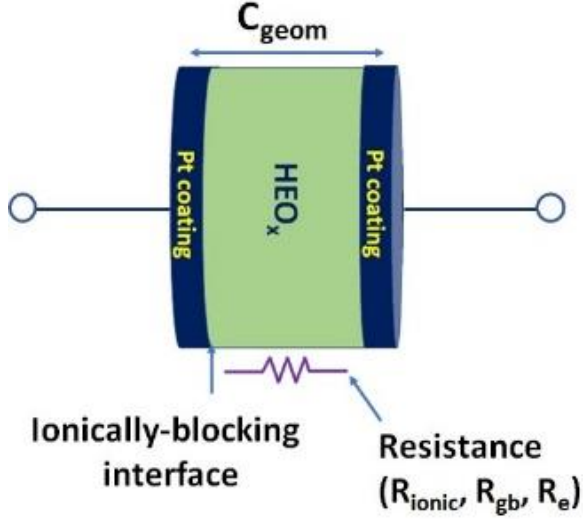


Fig.S14. The scheme for sample configuration for measurements and possible contributions to transport properties is depicted.

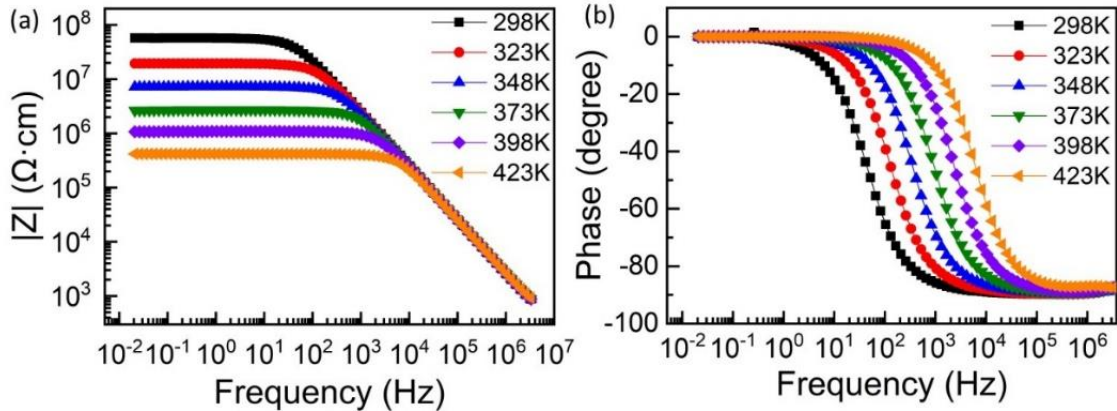


Fig.S15. (a) Modulus of impedance $|Z|$ and (b) phase as a function of frequency at different temperatures is shown for $\text{Zr}_{0.2}\text{Hf}_{0.2}\text{Ce}_{0.2}\text{Sn}_{0.2}\text{Mn}_{0.2}\text{O}_2$.

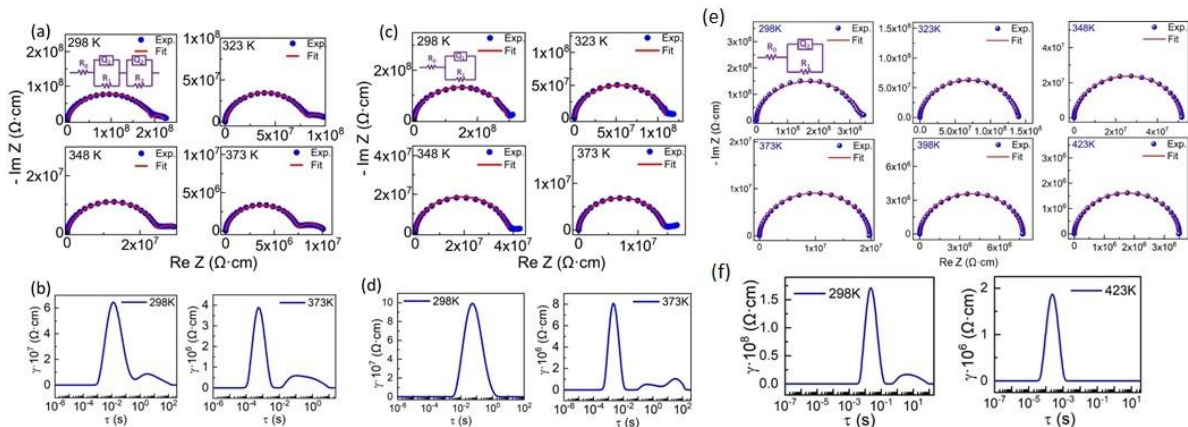


Fig. S16. Nyquist plots measured in the Pt/HEO_x/Pt configuration at different temperatures for (a) $\text{Zr}_{0.2}\text{Hf}_{0.2}\text{Ti}_{0.2}\text{Mn}_{0.2}\text{Ce}_{0.2}\text{O}_{2-\delta}$ (c) $\text{Zr}_{0.225}\text{Hf}_{0.225}\text{Ti}_{0.225}\text{Mn}_{0.225}\text{Ce}_{0.1}\text{O}_{2-\delta}$ and (e) $\text{Zr}_{0.2}\text{Hf}_{0.2}\text{Ti}_{0.2}\text{Mn}_{0.2}\text{Ce}_{0.1}\text{Ta}_{0.05}\text{Fe}_{0.05}\text{O}_{2-\delta}$. The Nyquist plot is fitted with the corresponding equivalent circuit as shown in the respective inset. The distribution of relaxation time (DRT) plots for (b) $\text{Zr}_{0.2}\text{Hf}_{0.2}\text{Mn}_{0.2}\text{Ce}_{0.2}\text{O}_{2-\delta}$ (d) $\text{Zr}_{0.225}\text{Hf}_{0.225}\text{Ti}_{0.225}\text{Mn}_{0.225}\text{Ce}_{0.1}\text{O}_{2-\delta}$ and (f) $\text{Zr}_{0.2}\text{Hf}_{0.2}\text{Ti}_{0.2}\text{Mn}_{0.2}\text{Ce}_{0.1}\text{Ta}_{0.05}\text{Fe}_{0.05}\text{O}_{2-\delta}$.

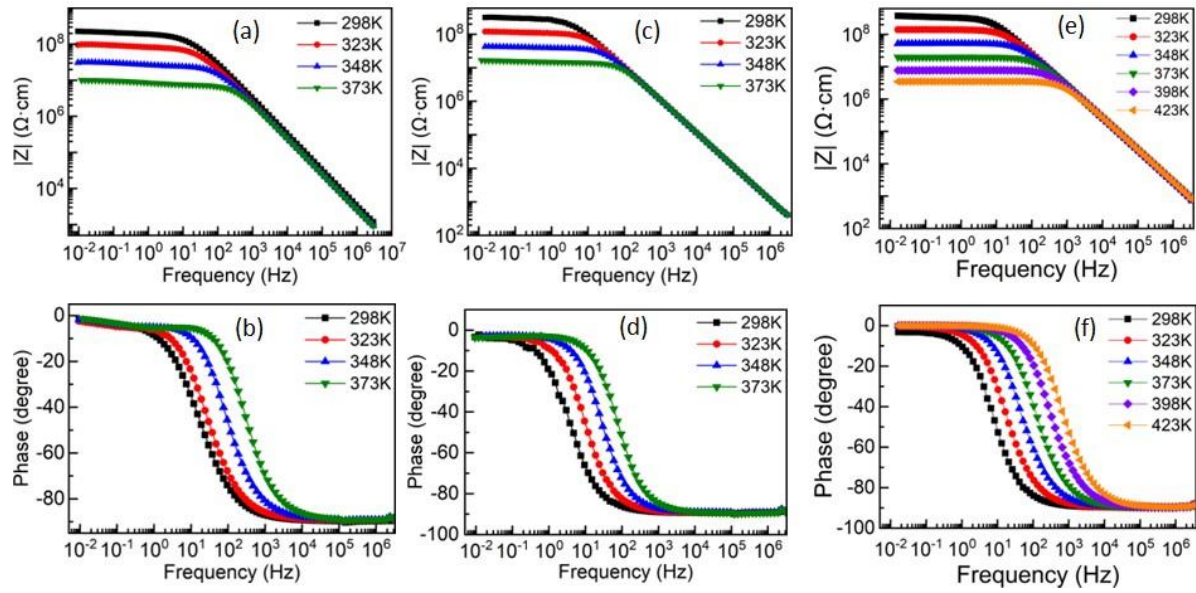


Fig.S17. Modulus of impedance $|Z|$ and phase as a function of frequency at different temperatures is shown for
 (a-b) $\text{Zr}_{0.2}\text{Hf}_{0.2}\text{Ti}_{0.2}\text{Mn}_{0.2}\text{Ce}_{0.2}\text{O}_2$ (c-d) $\text{Zr}_{0.225}\text{Hf}_{0.225}\text{Ti}_{0.225}\text{Mn}_{0.225}\text{Ce}_{0.1}\text{O}_2$, and (e-f)
 $\text{Zr}_{0.2}\text{Hf}_{0.2}\text{Ti}_{0.2}\text{Mn}_{0.2}\text{Ce}_{0.1}\text{Ta}_{0.05}\text{Fe}_{0.05}\text{O}_2$.

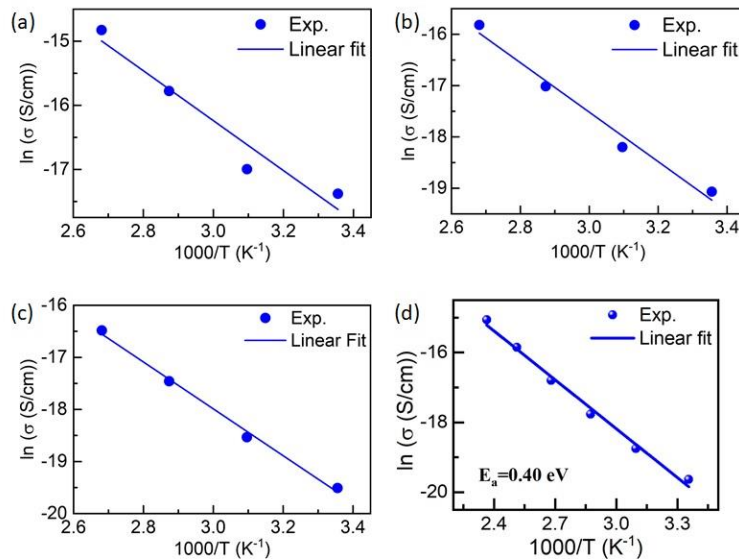


Fig.S18. Arrhenius plot for (a-b) $\text{Zr}_{0.2}\text{Hf}_{0.2}\text{Ti}_{0.2}\text{Mn}_{0.2}\text{Ce}_{0.2}\text{O}_2$, (c) $\text{Zr}_{0.225}\text{Hf}_{0.225}\text{Ti}_{0.225}\text{Mn}_{0.225}\text{Ce}_{0.1}\text{O}_2$ and (d)
 $\text{Zr}_{0.2}\text{Hf}_{0.2}\text{Ti}_{0.2}\text{Mn}_{0.2}\text{Ce}_{0.1}\text{Ta}_{0.05}\text{Fe}_{0.05}\text{O}_2$.

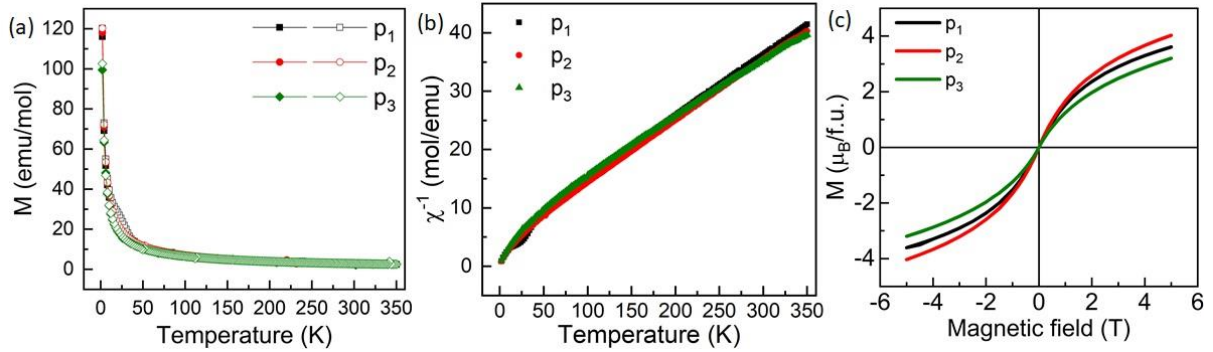


Fig.S19. (a) M-T curve in ZFC (filled symbol) and FC (open symbol) mode at 100 Oe, (b) χ^{-1} vs T curve and (c) M-H curve at 2K for entropy-stabilized fluorite oxides. p₁: $Zr_{0.2}Hf_{0.2}Ti_{0.2}Mn_{0.2}Ce_{0.2}O_2$, p₂: $Zr_{0.225}Hf_{0.225}Ti_{0.225}Mn_{0.225}Ce_{0.1}O_2$ and p₃: $Zr_{0.2}Hf_{0.2}Ti_{0.2}Mn_{0.2}Ce_{0.1}Ta_{0.05}Fe_{0.05}O_2$.

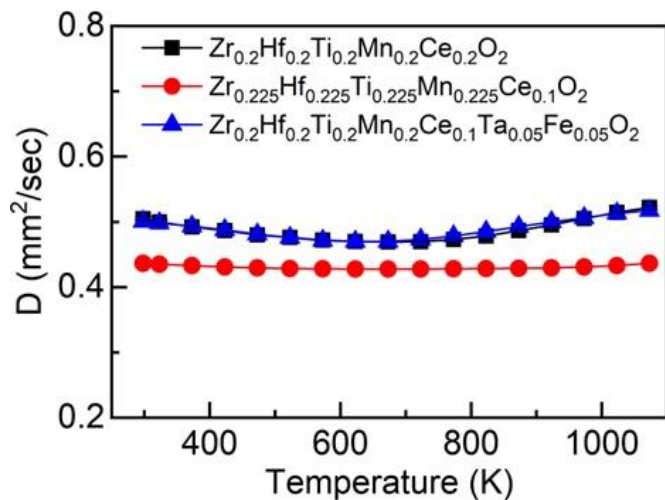


Fig.S20. Thermal diffusivity (D) measured using laser flash analysis (LFA) technique for all the three samples.

Table S1: Oxide precursors used for the synthesis of fluorite samples.

Oxide	Purity	Company Name	Structure	Coordination number	Cation ionic radius (Å)
ZrO ₂	99.9%	Alfa Aesar	Monoclinic	7	0.78
HfO ₂	99.9%	Alfa Aesar	Monoclinic	7	0.76
CeO ₂	99.9%	Alfa Aesar	Cubic	8	0.97
TiO ₂	99.9%	Alfa Aesar	Tetragonal	6	0.605
SnO ₂	99.9%	Alfa Aesar	Tetragonal	6	0.69
MnO ₂	99.9%	Alfa Aesar	Tetragonal	6	0.83(2+)
Fe ₂ O ₃	99.9%	Alfa Aesar	Monoclinic	6	0.645 (HS)
Ta ₂ O ₅	99.9%	Alfa Aesar	Orthorhombic	6	0.64
Y ₂ O ₃	99.9%	Alfa Aesar	Cubic	6	0.9

Table S2: The binding energies for each element corresponding to their oxidation state are listed.

Element	Peak positions		Ref.
Ce	See Table S4		[1-4]
Zr	3d _{5/2} : 182.1 eV	3d _{3/2} : 184.5 eV	[5]
Hf	4f _{7/2} : 16.7 eV	4f _{5/2} : 18.3 eV	[6]
Sn	3d _{5/2} : 486.1 eV	3d _{3/2} : 494.5 eV	[1]
Ti	2p _{3/2} : 458.5 eV	2p _{1/2} : 464.2 eV	[1]
Mn	See Fig. S8, Table S3		[7]
Ta	4f _{7/2} : 25.9 eV	4f _{5/2} : 27.8 eV	[1]
Fe	2p _{3/2} : 711.2 eV	2p _{1/2} : 725.5 eV	[1]

Table S3: The details of Ce-3d core-level fitting for Zr_{0.2}Hf_{0.2}Ti_{0.2}Sn_{0.2}Ce_{0.2}O₂.

Name	Peak BE eV	FWHM eV	Area (P) CPS.eV	Area (N) KE^0.6	Atomic %
Ce3d _{5/2} v	882.36	2.3	21892.19	15.39	12.32
Ce3d _{3/2} u	900.71	2.3	13856.25	14.33	11.47
Ce3d _{5/2} v''	888.88	2.61	3581.33	2.53	2.03
Ce3d _{3/2} u''	907.55	2.61	3767.66	3.92	3.14
Ce3d _{5/2} v'''	898.24	2.29	11778.98	8.41	6.74
Ce3d _{3/2} u'''	916.5	2.29	8989.58	9.45	7.57
Ce3d _{5/2} v0	880.49	2.2	12786.07	8.97	7.18
Ce3d _{3/2} u0	898.59	2.2	7777.55	8.03	6.43
Ce3d _{5/2} v'	885.3	3.62	39130.49	27.59	22.09
Ce3d _{3/2} u'	903.7	3.62	25331.18	26.28	21.04

Table S4: The details of Mn-2p fitting for Zr_{0.2}Hf_{0.2}Ti_{0.2}Mn_{0.2}Ce_{0.2}O_{2-δ}.

Name	Peak BE eV	FWHM eV	Area (P) CPS.eV	Area (N) KE^0.6	Atomic %
Mn2p Peak1	640.46	1.29	15662.64	19.73	29.37
Mn2p Peak2	641.48	1.29	14538.19	18.32	27.28
Mn2p Peak3	642.38	1.24	9017.96	11.37	16.94
Mn2p Peak4	643.16	1.20	4359.82	5.50	8.19
Mn2p Peak5	644.24	1.39	2125.61	2.68	4.00
Mn2p sat	646.28	3.42	7550.11	9.55	14.22

Table S5: The parameters obtained from the ZARC fitting of Nyquist plot for $Zr_{0.2}Hf_{0.2}Ce_{0.2}Sn_{0.2}Mn_{0.2}O_2$.

	R1 ($\Omega \cdot \text{cm}$)	T1	N1
298K	5.60E7±0.1%	3.99E-3±0.2%	0.95±0.1%
323K	1.93E7±0.1%	1.34E-3±0.2%	0.95±0.1%
348K	7.16E6±0.1%	4.9E-4±0.2%	0.96±0.1%
373K	2.68E6±0.1%	1.82E-4±0.1%	0.96±0.1%
398K	1.08E6±0.1%	7.2E-5±0.1%	0.96±0.1%
423K	4.17E5±0.1%	2.79E-5±0.1%	0.96±0.1%

Table S6: The parameters obtained from the ZARC fitting of Nyquist plot for $Zr_{0.2}Hf_{0.2}Ti_{0.2}Mn_{0.2}Ce_{0.2}O_2$.

	R1 ($\Omega \cdot \text{cm}$)	T1	N1	R2 ($\Omega \cdot \text{cm}$)	T2	N2
298K	1.81E8±1.4%	1.28E-2±1.2%	0.87±0.5%	5.18E7±6.7%	1.07±10.7%	0.56±5.6%
323K	7.71E7±0.6%	6.81E-3±0.4%	0.91±0.3%	2.90E7±0.3%	1.29±4.4%	0.56±3.1%
348K	2.35E7±0.3%	1.92E-3±0.2%	0.94±0.2%	9.47E6±2.7%	0.53±4.7%	0.57±2.2%
373K	7.37E6±2.0%	5.71E-4±2.0%	0.95±0.3%	2.40E6±2.1%	1.51E-1±2%	0.72±1.7%

Table S7: The parameters obtained from the ZARC fitting of Nyquist plot for $Zr_{0.225}Hf_{0.225}Ti_{0.225}Mn_{0.225}Ce_{0.1}O_2$.

	R1 ($\Omega \cdot \text{cm}$)	T1	N1
298K	3.04E8±0.3%	5.51E-2±0.9%	0.9±0.5%
323K	1.13E8±0.4%	1.94E-2±1.4%	0.9±0.7%
348K	4.07E7±0.4%	6.67E-3±1.7%	0.9±0.9%
373K	1.44E7±0.6%	2.25E-3±2.8%	0.9±0.8%

Table S8: The parameters obtained from the ZARC fitting of Nyquist plot for $Zr_{0.2}Hf_{0.2}Ti_{0.2}Mn_{0.2}Ce_{0.1}Ta_{0.05}Fe_{0.05}O_2$.

	R1 ($\Omega \cdot \text{cm}$)	T1	N1
298K	3.37E8±0.3%	2.40E-2±0.9%	0.92±0.4%
323K	1.39E8±0.6%	9.84E-3±0.2%	0.93±0.1%
348K	5.18E7±0.1%	3.57E-3±0.2%	0.95±0.1%
373K	1.98E7±0.1%	1.34E-3±0.1%	0.94±0.1%
398K	7.70E6±0.1%	5.27E-4±0.1%	0.95±0.1%
423K	3.50E6±0.1%	2.37E-4±0.1%	0.95±0.1%

References:

1. A. Pfau and K. D. Schierbaum, *Surf Sci*, 1994, **321**, 71–80.
2. E. Paparazzo, *Mater Res Bull*, 2011, **46**, 323–326.
3. L. Qiu, F. Liu, L. Zhao, Y. Ma and J. Yao, *Appl Surf Sci*, 2006, **252**, 4931–4935.
4. M. Romeo, K. Bak, J. el Fallah, F. le Normand and L. Hilaire, *Surface and Interface Analysis*, 1993, **20**, 508–512.
5. https://srdata.nist.gov/xps/main_search_menu.aspx
6. C. Morant, L. Galan, J. M. Sanz, *Surface and Interface Analysis* 1990, **16**, 304-308.
7. M. C. Biesinger, B. P. Payne, A. P. Grosvenor, L. W. M. Lau, A. R. Gerson, R. St. C. Smart, *Appl. Surf. Sci.* 2011, **257**, 2717.